Available online at www.sciencedirect.com
SCIENCE DIRECT®
PERGAMON
International Journal of Heat and Mass Transfer 46 (2003) 2155–2168
International Journal of HEAT and MASS TRANSFER
www.elsevier.com/locate/ijhmt

Numerical technique for modeling conjugate heat transfer in an electronic device heat sink

Andrej Horvat [a,*], Ivan Catton [b,1]

[a] Reactor Engineering Division, "Jožef Stefan" Institute, Jamova 39, SI-1111, Ljubljana 1000, Slovenia
[b] Mechanical and Aerospace Engineering Department, The Henry Samueli School of Engineering and Applied Science, University of California at Los Angeles, 48-121 Engineering IV Bldg., 420 Westwood Plaza, CA 90095-1597, Los Angeles, USA

Received 7 October 2002

Abstract

A fast running computational algorithm based on the volume averaging technique (VAT) is developed to simulate conjugate heat transfer process in an electronic device heat sink. The goal is to improve computational capability in the area of heat exchangers and to help eliminate some of empiricism that leads to overly constrained designs with resulting economic penalties.

VAT is tested and applied to the transport equations of airflow through an aluminum (Al) chip heat sink. The equations are discretized using the finite volume method (FVM). Such computational algorithm is fast running, but still able to present a detailed picture of temperature fields in the airflow as well as in the solid structure of the heat sink. The calculated whole-section drag coefficient, Nusselt number and thermal effectiveness are compared with experimental data to verify the computational model and validate numerical code. The comparison also shows a good agreement between FVM results and experimental data.

The constructed computational algorithm enables prediction of cooling capabilities for the selected geometry. It also offers possibilities for geometry improvements and optimization, to achieve higher thermal effectiveness.

1. Introduction

Heat exchangers are found in a number of different industrial sectors where the need to transport heat from medium to medium exists. They also have an important role in everyday life as they are one of the basic elements of heating, cooling, refrigerating and air-conditioning installations. Despite the crucial role of heat exchangers, there is still a lot of empiricism involved in their design. Although present-day guidelines provide ad-hoc solutions to the design problems, a unified approach based on simultaneous modeling of thermal hydraulics and structural behavior has not yet been developed and utilized. As a consequence, designs are overly constrained, with resulting economic penalties. Therefore, the optimization of a heat exchanger design can bring significant cost reductions to industry.

The objective of our work is to develop a unified, fast running, numerical algorithm for the calculation of heat exchanger morphologies using hierarchic modeling of the coolant and structure thermal behavior.

In the past, heat exchanger development was clearly dominated by interests of the military and power industries [1]. As the amount of heat transported through heat exchangers is the highest in nuclear installations, steam generators and heat exchangers in nuclear power reactors have been the focus of researchers' attention. This is the reason why the most experimental work was done with isothermal circular tubes [2–7,9] etc. Although some of the work is very comprehensive [6,7], most of these studies favored a circular geometry and did not include any other form of internal structure.

* Corresponding author. Tel.: +386-1-58-85-450; fax: +386-1-56-12-335/258.
E-mail address: andrej.horvat@ijs.si (A. Horvat).
[1] Tel.: +1-310-825-5320; fax: +1-310-206-4830.

0017-9310/03/$ - see front matter
doi:10.1016/S0017-9310(02)00532-X

Nomenclature

A_c	flow contact area of the test section
A_g	heat sink ground area
A_o	interface area in REV
$A_\perp$	area perpendicular to flow in the channel
c	specific heat
C_d	drag coefficient
d	pin-fins diameter
$d_h = 4V_f/A_c$	hydraulic diameter
FVM	finite volume method
g	arbitrary function
h	arbitrary function, heat transfer coefficient
H	height
H_b	height of the solid base-plate
L	length of the test section
p	pressure
p_x	pitch between pin-fins in x-direction
p_y	pitch between pin-fins in y-direction
Δp	pressure drop across the whole test section
REV	representative elementary volume
Q	heat flow
$Re_h = \bar{u}d_h/\nu_f$	Reynolds number
$S = A_o/V$	specific surface
t	time
T	temperature
T_g	ground temperature, $z = -H_b$ position
T_{if}	bottom temperature, $z = 0$ position
T_{in}	inflow temperature, $x = 0$ position
T_{out}	outflow temperature, $x = L$ position
u	streamwise velocity
v	velocity vector
V	representative elementary volume
V_k	volume occupied by phase k
W	width of the test section, mechanical work
x	general spatial coordinate, streamwise coordinate
y	horizontal spanwise coordinate
z	vertical spanwise coordinate

Greek symbols

α	volume fraction
β	arbitrary scalar
λ	thermal diffusivity
Λ	area of integration
μ	dynamic viscosity
ν	kinematic viscosity
ρ	density
Ω	volume of integration

Subscripts/superscripts

b	base
f	fluid phase
k	phasic variable
i, j	indexes
s	solid phase

Symbols

$\langle\ \rangle$	interphase average
$\bar{}$	intraphase average
$'$	discrepancy from the intraphase average

During the past few years, the electronics industry has been demanding more and more efficient heat exchanger designs. In particular, the speed of electronic chips is seriously bounded by the thermal power that the chips produce. As a consequence, electronic chips have to be intensively cooled using specially designed heat exchangers submerged into air or water flow [9–14]. In contrast to the previous case, where the heat exchanging structures are isothermal, the heat exchangers in the electronics industry consist mostly of highly conducting materials. This further complicates numerical calculations as well as experimental work due to the conjugate nature of heat transfer [15].

The widespread use of heat exchangers across many industrial sectors has caused their development to take place in a piecemeal fashion in a number of rather unrelated areas. Much of the technology, familiar in one sector, moved only slowly over the boundaries into another sector [16]. To overcome historic differences, a unified description for fluid and heat flow through a solid matrix has to be found. One of the suitable options is the volume averaging technique (VAT), where transport processes in a heat exchanger are modeled as porous media flow [17]. This generalization allows us to unify the heat transfer calculation techniques for different kinds of heat exchangers and their structures. The case-specific geometrical arrangements, material properties and fluid flow conditions enter the computational algorithm only as a series of precalculated coefficients. This clear separation between the model and the case-specific coefficients simplifies the procedure to determine the optimum heat transfer conditions.

In this work, attention will be focused on volume averaging and on the underlying VAT. Applying VAT, the flow variables are averaged over a representative elementary volume (REV). The variations, which occur on a scale smaller than the averaged volume, have to be modeled separately in the form of closure models. Although the details of the modeled flow are lost due to the averaging procedure, the hierarchical modeling principle of VAT represents a theoretically rigorous methodology for simulation of multi-component flow systems.

The VAT was initially proposed in the 1960s by Anderson and Jackson [18], Slattery [19], Marle [20], Whitaker [21] and Zolotarev and Redushkevich [22]. Many of the important details and examples of applications can be also found in books by Dullien [23], Kheifets and Neimark [24], and Adler [25]. The method was expanded to problems of turbulent transport in porous media by Primak et al. [26], Sheherban et al. [27], Travkin et al. [28–30] and Travkin and Catton [31–33]. Travkin and Catton [33] also worked further on development of VAT for heterogeneous media applicable to non-linear physical phenomena in thermal science and fluid mechanics. Their mathematically strict derivation of porous media transport equations also represents the theoretical foundation of this work.

The design of heat exchangers is a well-studied subject due to its importance. Nevertheless, the proposed VAT, which is based on rigorous scientific methodology, has rarely been applied to conjugate heat transfer problems in heat exchangers. Therefore, the article presents the VAT formulation and solution of conjugate heat transfer problem for an aluminum (Al) heat sink used as an electronics cooling device.

2. Volume averaging technique (VAT)

The fluid-structure interaction and heat transfer in a heat exchanger can be described with basic mass, momentum and heat transport equations. For a model to have short computing times, the transport equations are averaged over a REV as presented in Fig. 1. The method produces porous media flow equations, where each phase and its properties are separately defined over the whole simulation domain. In order to understand the model and its results, the theoretical foundations of VAT must be given.

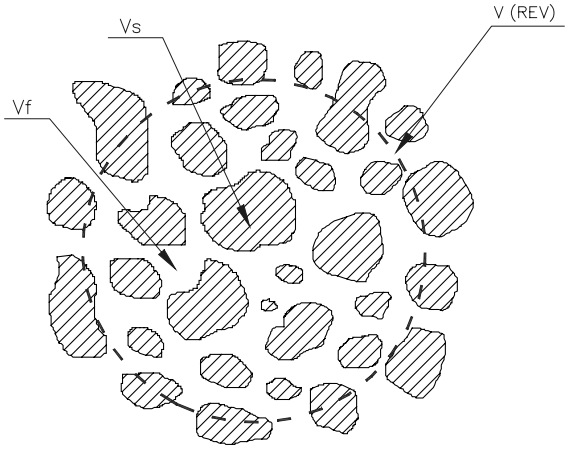

Fig. 1. Averaging over REV.

In the present work, the phase k fraction is defined as the ratio between the portion of the REV occupied by phase k and the total REV:

$$\alpha_k = \frac{V_k}{V}. \tag{1}$$

In the following developments, two kinds of averaging are used. If the variable h, which is defined in the phase k is averaged over the total REV (Eq. (2)), the expression "interphase average" is used,

$$\langle h\rangle_k = \langle h_k\rangle = \frac{1}{V}\int_{V_k} h\,\mathrm{d}\Omega. \tag{2}$$

More convenient is to use the average of the variable h over the phase k control volume V_k (Eq. (3)). In this case, the expression "intraphase average" is used.

$$\bar{h}_k = \frac{1}{V_k}\int_{V_k} h\,\mathrm{d}\Omega, \tag{3}$$

where $h' = h - \bar{h}_k$. Thus h' is defined as a discrepancy from the intraphase average $\bar{h}_k$ in the volume V_k which is occupied by the phase k. From the definitions (2) and (3), the relationship between interphase and intraphase average is

$$\langle h\rangle_k = \alpha_k \bar{h}_k. \tag{4}$$

When the phase-interface is fixed in space, the volume averaging is a linear operator:

$$\langle h+g\rangle_k = \langle h\rangle_k + \langle g\rangle_k, \tag{5}$$

$$\langle \beta h\rangle_k = \beta\langle h\rangle_k$$

and

$$\overline{(h+g)}_k = \bar{h}_k + \bar{g}_k, \tag{6}$$

$$\overline{(\beta h)}_k = \beta\bar{h}_k.$$

where h and g are two independent function and β is a constant.

If the composition of the considered multiphase medium is steady, the average of the time derivative can be treated as

$$\left\langle \frac{\partial h}{\partial t}\right\rangle_k = \frac{\partial}{\partial t}\langle h\rangle_k \quad \text{and} \quad \overline{\left(\frac{\partial h}{\partial t}\right)}_k = \frac{\partial}{\partial t}\bar{h}_k. \tag{7}$$

Applying volume averaging to a spatial derivative produces two terms:

$$\left\langle \frac{\partial h}{\partial x_j}\right\rangle_k = \frac{\partial}{\partial x_j}\langle h\rangle_k + \frac{1}{V}\int_{A_o} h\,\mathrm{d}\Lambda_j \quad \text{and}$$

$$\overline{\left(\frac{\partial h}{\partial x_j}\right)}_k = \frac{\partial}{\partial x_j}\bar{h}_k + \frac{1}{V_k}\int_{A_o} h'\,\mathrm{d}\Lambda_j, \tag{8}$$

where the last term in both cases is an interface exchange term.

Using the VAT basic rules (1)–(8), the mass, momentum and energy transport equations are developed for laminar steady-state flow in porous media. The index f, when marking intraphase average velocity, is omitted to avoid double indexing.

When the spatial differential rule (8) together with Eq. (4) is applied, the mass transport equation can be written as:

$$\alpha_f \frac{\partial \bar{v}_i}{\partial x_i} = 0. \tag{9}$$

The derivation of the momentum transport equation for porous media flow starts from the momentum equation for steady-state incompressible flow, where the effect of gravity is neglected. As the considered solid structure is uniform in space, the phase fraction α_f is constant, allowing one to write:

$$\alpha_f \rho_f \bar{v}_j \frac{\partial \bar{v}_i}{\partial x_j} = -\alpha_f \frac{\partial \bar{p}_f}{\partial x_i} + \alpha_f \mu_f \frac{\partial^2 \bar{v}_i}{\partial x_j^2} - \frac{1}{V}\int_{A_o} p \, \mathrm{d}A_i + \frac{\mu_f}{V}\int_{A_o} \frac{\partial v_i}{\partial x_j}\, \mathrm{d}A_j. \tag{10}$$

The integrals in Eq. (10) are a consequence of the volumetric averaging. They capture momentum transport on the fluid–solid interface. As in turbulent flow, a separate model in the form of a closure relation is needed. In the present case, the integrals are replaced with the following empirical drag relation,

$$-\int_{A_o} p \, \mathrm{d}A_i + \mu_f \int_{A_o} \frac{\partial v_i}{\partial x_j}\, \mathrm{d}A_j = \frac{1}{2} C_d \rho_f \bar{v}_i^2 A_o, \tag{11}$$

where C_d is a drag coefficient that depends on a local Reynolds number. Inserting the empirical correlation (11) into Eq. (10), the momentum equation for porous media flow is given by

$$\alpha_f \rho_f \bar{v}_j \frac{\partial \bar{v}_i}{\partial x_j} = -\alpha_f \frac{\partial \bar{p}_f}{\partial x_i} + \alpha_f \mu_f \frac{\partial^2 \bar{v}_i}{\partial x_j^2} + \frac{1}{2} C_d \rho_f \bar{v}_i^2 S, \tag{12}$$

where S is the specific surface of the structure.

The energy transport equation for the fluid phase is developed from the energy transport equation for steady-state incompressible flow. For uniform porous media, it is written as

$$\alpha_f \rho_f c_f \bar{v}_j \frac{\partial \overline{T}_f}{\partial x_j} = \alpha_f \lambda_f \frac{\partial^2 \overline{T}_f}{\partial x_j^2} + \frac{\lambda_f}{V}\int_{A_o} \frac{\partial T}{\partial x_j}\, \mathrm{d}A_j. \tag{13}$$

The integral term in Eq. (13) represents the interfacial heat exchange between the fluid flow and the solid structure and requires additional modeling. In the present case, an empirical linear relation between the fluid and the solid temperature is taken as an appropriate model for the interphase heat flow:

$$-\lambda_f \int_{A_o} \frac{\partial T}{\partial x_j}\, \mathrm{d}A_j = h(\overline{T}_f - \overline{T}_s) A_o, \tag{14}$$

where h is a heat transfer coefficient that depends on the local Reynolds number. By substituting the relation (14) into Eq. (13), the fluid flow energy transport equation can be written as:

$$\alpha_f \rho_f c_f \bar{v}_j \frac{\partial \overline{T}_f}{\partial x_j} = \alpha_f \lambda_f \frac{\partial^2 \overline{T}_f}{\partial x_j^2} - h(\overline{T}_f - \overline{T}_s) S. \tag{15}$$

In the solid phase, thermal diffusion is the only heat transport mechanism. Therefore, the energy transport equation is reduced to the simple diffusion equation:

$$0 = \alpha_s \lambda_s \frac{\partial^2 \overline{T}_s}{\partial x_j^2} + \frac{\lambda_s}{V}\int_{A_o} \frac{\partial T}{\partial x_j}\, \mathrm{d}A_j, \tag{16}$$

where the integral captures the interphase heat exchange. Closure is obtained by substituting the linear relation:

$$\lambda_s \int_{A_o} \frac{\partial T}{\partial x_j}\, \mathrm{d}A_j = h(\overline{T}_f - \overline{T}_s) A_o \tag{17}$$

in Eq. (16). The VAT energy transport equation for solid structure is then written as

$$0 = \alpha_s \lambda_s \frac{\partial^2 \overline{T}_s}{\partial x_j^2} + h(\overline{T}_f - \overline{T}_s) S. \tag{18}$$

3. Simulation setup

The geometry of the simulation domain follows the geometry of the experimental test section used in the Morrin-Martinelli-Gier Memorial Heat Transfer Laboratory at University of California, Los Angeles, where experimental data described in [34] were obtained.

The general arrangement of the heat sink is given in Fig. 2. The length L as well as the width W of the heat sink are 0.1143 m (4.5 in.), whereas the height H is 0.0381 m (1.5 in.). The conductive base plate, which connects pin-fins, is 0.00635 m (0.25 in.) high.

The heat sink solid structure, which is exposed to air cross-flow, consists of 31 rows of aluminum pin-fins in the streamwise (x-direction) and in the transverse direction (y-direction). The diameter of the pin-fins is $d = 0.003175$ m (0.125 in.). The pitch-to-diameter ratio in the streamwise direction is set to $p_x/d = 1.06$ and in the transverse direction to $p_y/d = 2.12$.

The material properties are also taken from the experimental cases. The heat sink consists of cast aluminum alloy 195. The entering flow profile is uniform due to two rows of honeycomb flow-straighteners that are placed in front of the test section. The heat sink is heated from bellow by an electric resistance heater. A thermal isolation layer placed between the heater and the aluminum base sets the isothermal conditions at the base bottom.

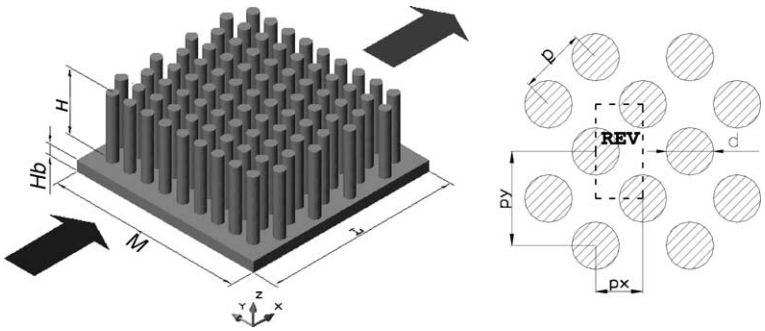

Fig. 2. Experimental test section with the pin-fins arrangement.

As the experimental data were taken at thermal power of 50, 125 and 220 W, the numerical simulations are performed at the same heating rates.

4. Governing equations for uniform flow through heat sink

The mathematical model of the flow through the heat sink is based on the description of porous media flow given in Section 2. It consists of a mass transport equation, a momentum transport equation, an energy transport equation for the fluid flow, an energy transport equation for the solid structure and an energy transport equation for the heat conductive base-plate. As all equation variables are already averaged over the appropriate REV, the averaging symbol $^-$ is omitted.

The momentum transport equation for fluid flow is developed from Eq. (12) with the additional assumption that the volume average velocity through the heat sink is unidirectional: $v = \{u, 0, 0\}$. As a consequence of continuity (Eq. (9)), the velocity varies only transversely to the flow direction. This means that the pressure force across the entire simulation domain is balanced with shear forces. As a result, the momentum transport equation is reduced to

$$-\alpha_f \mu_f \left(\frac{\partial^2 u}{\partial y^2} + \frac{\partial^2 u}{\partial z^2} \right) + \frac{1}{2} C_d \rho_f u^2 S = \frac{\Delta p}{L}. \tag{19}$$

In order to close the momentum equation (19), the local drag coefficient C_d has to be determined. In the present work, the experimental data from Launder and Massey [2] and Kays and London [1] are used to construct a correlation for the local drag coefficient C_d as a function of the local Reynolds number.

The boundary conditions for the model equations attempt to represent the experimental conditions described previously. For the momentum transport equation (19), no-slip boundary conditions are implemented at all four walls parallel to the flow direction:

$$\begin{aligned} u(0,z) &= 0, \quad u(W,z) = 0, \\ u(y,0) &= 0, \quad u(y,H) = 0. \end{aligned} \tag{20}$$

The input values of the whole-section pressure drop p are summarized in Table 1.

The energy transport equation for the fluid flow is developed from Eq. (15) with the unidirectional velocity assumption. The temperature field in the fluid results from a balance between thermal convection in the streamwise direction, thermal diffusion and the heat transferred from the solid structure to the fluid flow. Thus, the differential form of the energy equation for the fluid is:

$$\alpha_f \rho_f c_f u \frac{\partial \overline{T}_f}{\partial x} = \alpha_f \lambda_f \left(\frac{\partial^2 T_f}{\partial x^2} + \frac{\partial^2 T_f}{\partial y^2} + \frac{\partial^2 T_f}{\partial z^2} \right) - h(T_f - T_s)S. \tag{21}$$

A correlation based on the experimental data of Žukauskas and Ulinskas [8] are used for the local heat transfer coefficient h at low Reynolds numbers, whereas for higher Reynolds numbers, the experimental data from Kay and London [1] are more appropriate.

Table 1
Whole-section pressure drop Δp [Pa] at 50, 125 and 220 W

Calculation	1	2	3	4	5	6	7	8
Δp [Pa] at 50 W	5.0	10.0	20.0	40.0	74.72	175.6	266.5	368.6
Δp [Pa] at 125 W	5.0	10.0	20.0	40.0	74.72	179.3	274.0	361.1
Δp [Pa] at 220 W	5.0	10.0	20.0	40.0	74.72	180.6	280.2	361.1

Table 2
Inflow temperature T_{in} [°C] at 50, 125 and 220 W

Calculation	1	2	3	4	5	6	7	8
T_{in} [°C] at 50 W	23.0	23.0	23.0	23.0	23.02	23.02	23.04	22.85
T_{in} [°C] at 125 W	23.0	23.0	23.0	23.0	23.16	23.21	23.05	22.81
T_{in} [°C] at 220 W	23.0	23.0	23.0	23.0	23.07	22.96	22.97	22.90

Table 3
Solid base bottom temperature T_g [°C] at 50, 125 and 220 W

Calculation	1	2	3	4	5	6	7	8
T_g [°C] at 50 W	54.9	43.43	37.2	33.0	30.3	27.9	27.3	26.64
T_g [°C] at 125 W	103.8	74.6	58.8	48.15	41.8	35.73	33.6	32.25
T_g [°C] at 220 W	168.0	114.8	87.0	68.0	56.4	45.2	42.3	40.4

For the fluid-phase energy transport equation (21), the simulation domain inflow and the bottom wall are taken as isothermal:

$$T_f(0,y,z) = T_{in}, \quad T_f(x,y,0) = T_{if}(x,y,0) \tag{22}$$

whereas the other boundary conditions are adiabatic:

$$\begin{aligned} &\frac{\partial T_f}{\partial x}(L,y,z) = 0, \quad \frac{\partial T_f}{\partial y}(x,0,z) = 0, \\ &\frac{\partial T_f}{\partial y}(x,W,z) = 0, \quad \frac{\partial T_f}{\partial z}(x,y,H) = 0, \end{aligned} \tag{23}$$

The inflow boundary values T_{in} of the fluid temperature T_f are summarized in Table 2. It has to be noted that the bottom temperature T_{if} is influenced by a temperature distribution in the conductive base-plate and is therefore position dependent.

The energy transport equation for the solid structure is developed from Eq. (18). The heat sink structure in each REV is not connected in horizontal directions (Fig. 2). As a consequence, only the thermal diffusion in the vertical direction is in balance with the heat leaving the structure through the fluid–solid interface, whereas the thermal diffusion in the horizontal directions can be neglected. This simplifies the energy equation for the solid structure to:

$$0 = \alpha_s \lambda_s \frac{\partial^2 T_s}{\partial z^2} + h(T_f - T_s)S. \tag{24}$$

For the solid-phase energy transport equation (24), the bottom wall is prescribed as isothermal, whereas the top wall is assumed to be adiabatic:

$$T_s(x,y,0) = T_{if}(x,y,0), \quad \frac{\partial T_s}{\partial z}(x,y,H) = 0. \tag{25}$$

The energy transport equation in the solid base-plate is developed from Eq. (18). As there is no heat transfer between solid and fluid phase except at the upper boundary, the interphase heat exchange term is omitted. Therefore, the energy transport equation reduces to the three-dimensional thermal diffusion equation:

$$0 = \lambda_s \left(\frac{\partial^2 T_b}{\partial x^2} + \frac{\partial^2 T_b}{\partial y^2} + \frac{\partial^2 T_b}{\partial z^2} \right). \tag{26}$$

The boundary conditions for the solid base-plate show the coupled nature of heat transfer between the porous media flow, Eqs. (21) and (24), and the base, Eq. (26). Namely, the heat flux at the interface between porous media and the base must be equal:

$$\lambda_s \frac{\partial T_b}{\partial z}(x,y,0) = \alpha_f \lambda_f \frac{\partial T_f}{\partial z}(x,y,0) + \alpha_s \lambda_s \frac{\partial T_s}{\partial z}(x,y,0). \tag{27}$$

The calculated temperature T_b at the boundary is equal to the temperature T_{if}, which is used as the boundary condition (22) and (25) in the energy transport equations (21) and (24). At the base-plate bottom, isothermal boundary conditions are prescribed

$$T_b(x,y,-H_b) = T_g, \tag{28}$$

whereas the horizontal walls are taken as adiabatic:

$$\begin{aligned} &\frac{\partial T_b}{\partial x}(0,y,z) = 0, \quad \frac{\partial T_b}{\partial x}(L,y,z) = 0, \\ &\frac{\partial T_b}{\partial y}(x,0,z) = 0, \quad \frac{\partial T_b}{\partial y}(x,W,z) = 0. \end{aligned} \tag{29}$$

The bottom boundary values T_g for the base temperature T_b are summarized in Table 3.

5. Solution methods

The developed transport equations (19), (21), (24) and (26) as well as the appropriate boundary conditions (20), (22), (23), (25), (27)–(29) are transformed into dimensionless form. Namely, the dimensionless form eases identification of different mechanisms as well as comparison of results with other authors. Moreover, the

dimensionless form of equations also enables one to use more general numerical algorithms that are already developed and are publicly accessible.

The dimensionless transport equations are then discretized following principles of the finite volume method (FVM) [35]. The momentum transport equation (19) with the boundary conditions (20) is discretized using the central-difference scheme in both spanwise directions (y and z). Although the resulting five-diagonal matrix is symmetrical, it has non-constant terms on the central diagonal, due to the non-linear drag force term.

Similarly, the energy transport equation for fluid flow (21) with the boundary conditions (22) and (23) is discretized in all three dimensions (x, y and z) using the central-difference scheme for the diffusion terms and the upwind scheme for the convection term, respectively. In this case, the resulting seven-diagonal matrix system is not symmetrical, due to the upwind discretization of the convection term, nor does it have constant terms, due to the locally changing heat transfer coefficient h.

The energy transport equation for the solid structure (24) with the boundary conditions (25) is discretized in the vertical direction (z) using the central-difference scheme. The resulting three-diagonal matrix is symmetric with varying diagonal terms as a result of local variations in the heat transfer coefficient h.

The central-difference scheme is also used to discretize the energy diffusion transport equation for the solid base-plate (26) and its boundary conditions (27)–(29) in all three-dimensions (x, y and z). The resulting seven-diagonal matrix is basically symmetrical. Nevertheless, the symmetry is spoiled due to the coupled boundary conditions at the top boundary.

The three-, five- and seven-diagonal asymmetric matrix systems of discrete non-linear equations are solved with an iteration procedure, where the precondition conjugate gradient (PCG) method is applied as an elliptic-hyperbolic equation solver. The detailed description of PCG method can be found in Ferziger and Perić [36].

6. Results

Simulations of the heat sink thermal behavior were performed for 8 different pressure drops Δp and boundary temperatures T_{in} and T_g, which are summarized in Tables 1–3. Three sets of calculations were carried out for heating power of 50, 125 and 220 W to match the experimental data obtained by Rizzi et al. [34]. To calculate velocity and temperature fields in airflow and in the solid structure, $31 \times 15 \times 140$ finite volumes were used in x-, y - and z-direction, respectively. For simulation of diffusion heat transfer in the solid base-plate the same number of finite volumes were employed.

6.1. Comparison of whole-section values

The imposed pressure drop Δp causes airflow through the heated solid structure. As the structure is cooled, a steady-state temperature field is formed in the airflow as well as in the thermal conductive aluminum. Based on the calculated velocity and temperature fields, the whole-section drag coefficient

$$\overline{C}_d = \frac{2\Delta p}{\rho_f u^2 LS}, \tag{30}$$

and the whole-section Nusselt number

$$\overline{Nu} = \frac{\overline{Q} d_h}{(T_g - T_{in}) A_g \lambda_f}, \tag{31}$$

are estimated as functions of Reynolds number Re_h, which is based on a hydraulic diameter d_h of a hypothetical porous media channel. Similarly, the thermal effectiveness $\overline{Q}/\overline{W}$, which is defined as the ratio between the heat transferred through the structure

$$\overline{Q} = \alpha_f \rho_f c_f \overline{u(T_{out} - T_{in})} A_\perp, \tag{32}$$

and the mechanical pumping power expended to overcome fluid friction

$$\overline{W} = \alpha_f \Delta p A_\perp \bar{u}, \tag{33}$$

is obtained from the calculated velocity and temperature fields.

The calculated whole-section values of the drag coefficient $\overline{C}_d$, Nusselt number $\overline{Nu}$ and thermal effectiveness $\overline{Q}/\overline{W}$ are compared with the experimental data, which were obtained in the Morrin-Martinelli-Gier Memorial Heat Transfer Laboratory at the University of California, Los Angeles [34]. As the experimental methods cannot provide a detailed picture of velocity and temperature fields, the comparisons of these whole-section values serve as the verification of the constructed physical model and validate the developed numerical code.

The consistency analysis of the developed model was also performed. For this purpose the simulations were done with 10, 20, 40, 80 and 160 grid points in the vertical (z-direction) for each separate phase: fluid flow, the solid structure and the solid base-plate. Based on the simulation results, the whole-section drag coefficient $\overline{C}_d$ and Nusselt number $\overline{Nu}$ were calculated for different Reynolds numbers. Fig. 3 presents only a part of results in order to prove consistency of the developed procedure. It is evident that the whole-section drag coefficient $\overline{C}_d$, obtained with 10 grid points, differs for 2% from the drag coefficient $\overline{C}_d$ calculated with 160 grid points (Fig. 3a). This relative difference is even smaller in the case of the whole-section Nusselt number $\overline{Nu}$ (Fig. 3b). It is interesting to note that the relative difference of the whole section drag coefficient $\overline{C}_d$ or Nusselt number $\overline{Nu}$

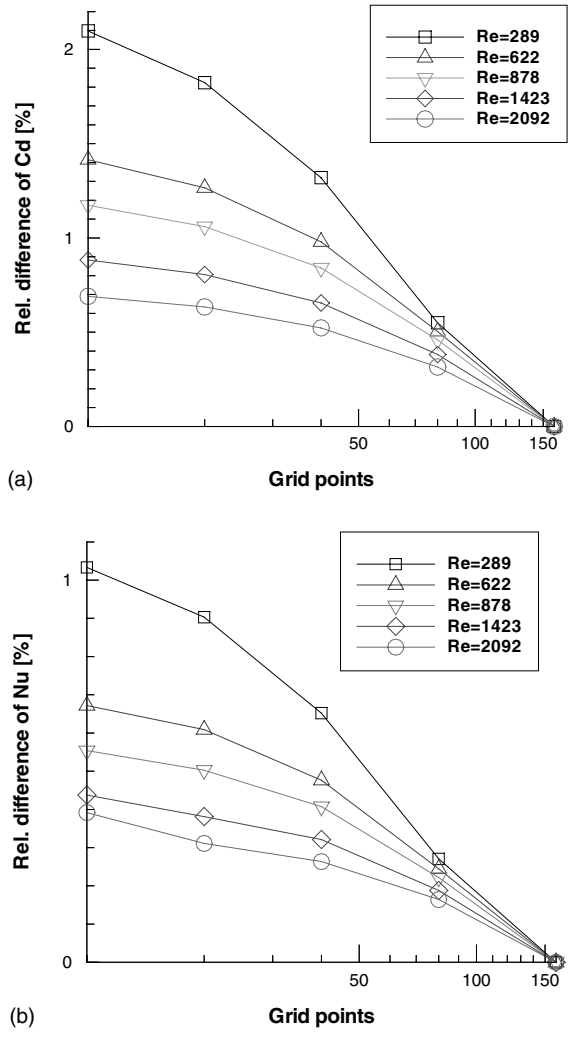

Fig. 3. Consistency analysis of the whole-section drag coefficient $\overline{C}_d$ (a) and Nusselt number $\overline{Nu}$ (b), $Q = 150$ W.

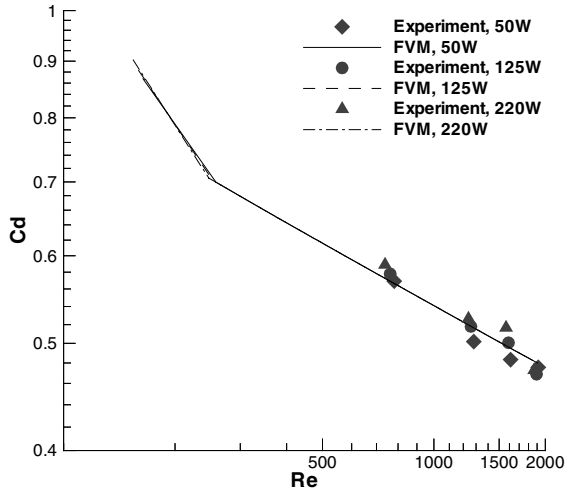

Fig. 4. Whole-section drag coefficient $\overline{C}_d$.

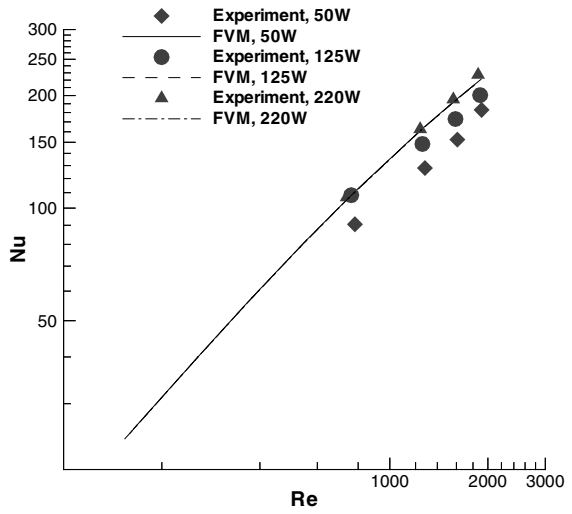

Fig. 5. Whole-section Nusselt number $\overline{Nu}$.

is higher at low than at high Reynolds number Re_h. Namely, with increasing Reynolds number a velocity profile is becoming more flat and it is less influenced by a number of grid points involved in the calculation.

Fig. 4 shows the whole-section drag coefficient $\overline{C}_d$ as a function of Reynolds number Re_h at thermal power of 50, 125 and 220 W. In general, the results calculated with FVM are close to experimental data. The scattering of the experimental data at higher Reynolds number is due to transition to turbulence, which is evident on experimental results, but is not captured by the model. The calculated values show only a slight difference at different level of thermal power due to temperature dependent material properties. At higher thermal power (e.g. 220 W), the airflow through the heat sink is strongly influenced by thermal stratification, due to intensive heating at the bottom. The resulting buoyancy effects cause model deficiencies as well as problems with representation of the collected experimental data.

Fig. 5 show the whole-section Nusselt number $\overline{Nu}$ as a function of Reynolds number Re_h at thermal power of 50, 125 and 220 W. The Nusselt number Nu distributions reveal larger difference between the FVM results and the experimental data. The difference of approximately 10% is steady throughout the whole range of tested Reynolds numbers, which is believed to be a consequence of systematic modeling or experimental error. As the thermal power is increased to 125 W, the FVM results display only minor difference of approximately 5% of experi-

mental values. At even higher thermal powers, the difference between calculated values and experimental data becomes negligible. As the difference cannot be observed at higher thermal power, it is suspected to be a consequence of systematic modeling or experimental error.

Fig. 6 shows the whole-section thermal effectiveness $\overline{Q}/\overline{W}$ as a function of Reynolds number Re_h at thermal power of 50, 125 and 220 W. In all three cases an excellent agreement between the FVM results and the experimental data is obtained. The thermal effectiveness $\overline{Q}/\overline{W}$ is increasing with increasing heat input and decreasing with increasing Reynolds number Re_h. Although, the lower Reynolds numbers bring higher thermal effectiveness, resulting low heat transfer rates have to be compensated with a larger heat transfer surface and consequently with larger size of a heat sink. In some cases this is not possible due to cost and size limitations.

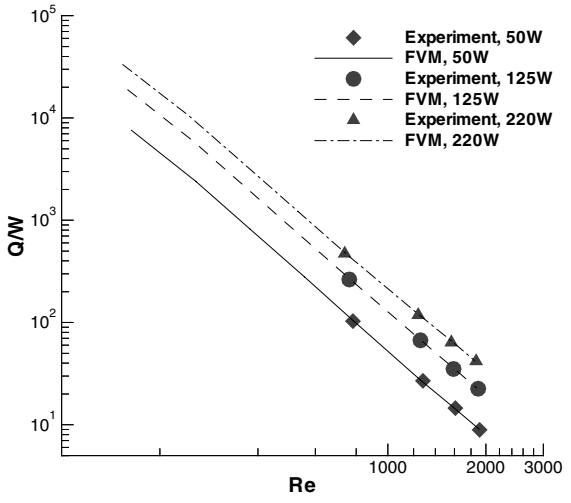

Fig. 6. Test section thermal effectiveness $\overline{Q}/\overline{W}$.

6.2. Temperature distribution in heat sink

The detailed temperature fields at different Reynolds numbers Re_h, give an insight into the heat transfer conditions in the studied heat sink. It should be also noted that although different heating power (50, 125 or 220 W) is used on the base-plate, there exists a similarity in force convection heat removal from the heat sink structure. Namely, higher heat input causes higher absolute temperature levels, whereas the form of isotherms changes only slightly, due to modification in air material properties. Therefore, this section presents the velocity profiles and temperature fields only for thermal power of 125 W.

Fig. 7 gives velocity profiles of airflow at the middle of the simulation domain ($y = 0.5$ W) at different Reynolds numbers Re_h. The core of the velocity profiles has a flat shape due to drag associated with submerged pin-fins. As the drag is smaller at lower Reynolds numbers Re_h, the boundary layer close to the bottom and the top is much more resolved.

Figs. 8–13 show the temperature field cross-sections at different Reynolds numbers Re_h. The temperatures are in Celsius scale. The cross-sections of temperature field are taken at the middle of the simulation domain, $y = 0.5$ W. Figures marked with (a) present the temperature field in the fluid flow, whereas figures marked with (b) reveal the temperature field in the solid structure and the base-plate.

It is evident that the lowest temperature in the airstream is at the beginning of the heat sink; this is on the left side. The temperature raises as the air passes through the heat exchanging structure. Therefore, the highest temperatures are expected at the exit; this is on the right side. The temperature field in the solid structure is more horizontally stratified, as the heat enters the structure from the bottom. As a consequence, the lowest temperature in the solid phase is in the upper left corner and the highest on the bottom, close to the base-plate.

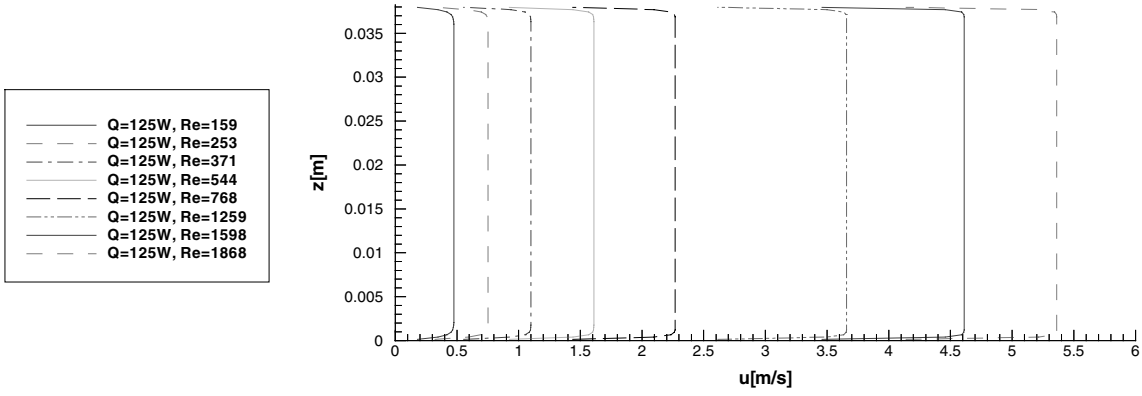

Fig. 7. Fluid velocity cross-section, $Q = 125$ W.

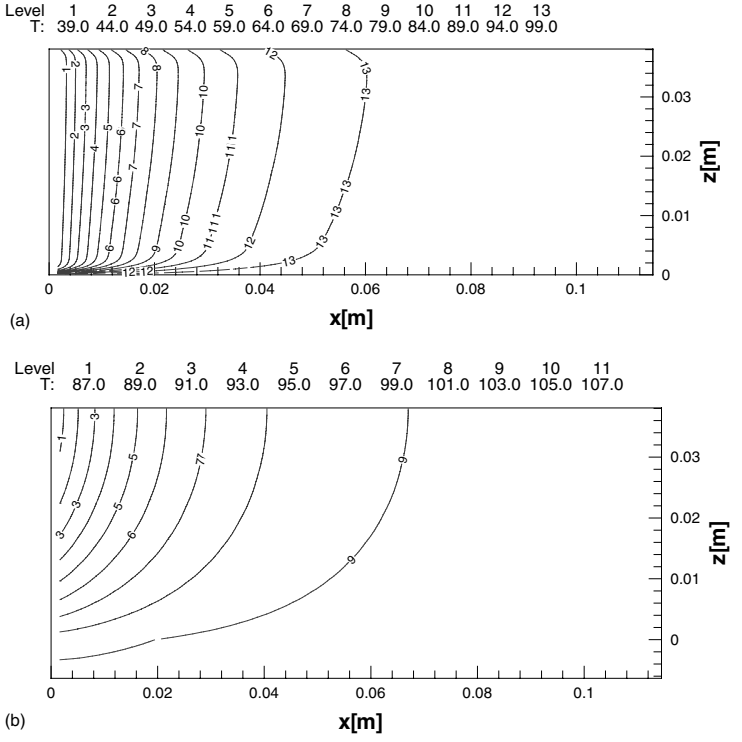

Fig. 8. Temperature field in the fluid (a) and in the solid (b), $Re_h = 159$, $Q = 125$ W.

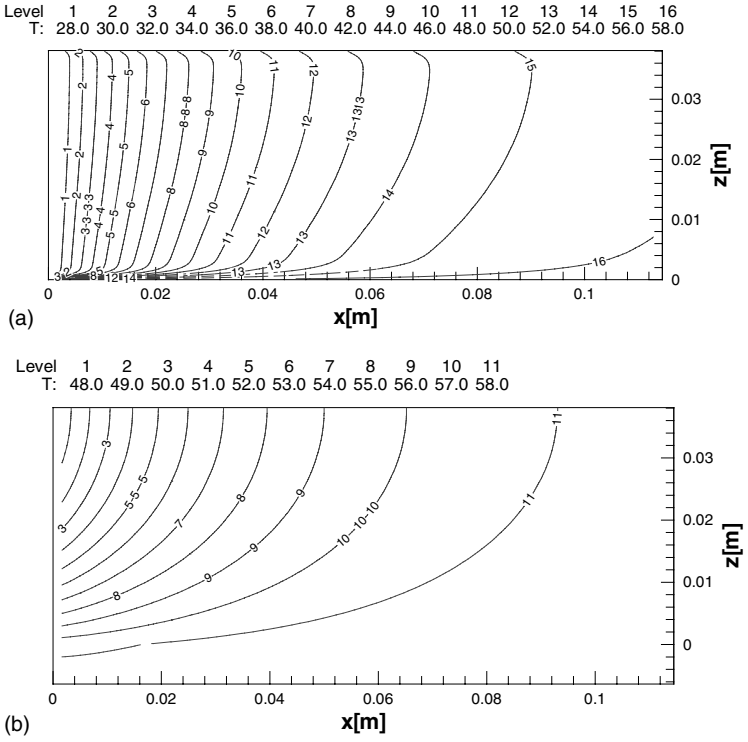

Fig. 9. Temperature field in the fluid (a) and in the solid (b), $Re_h = 371$, $Q = 125$ W.

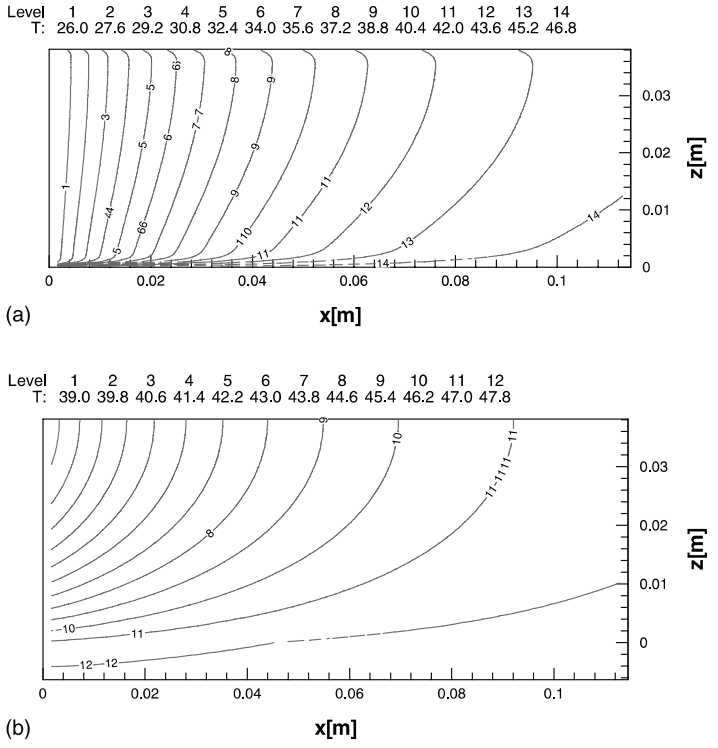

Fig. 10. Temperature field in the fluid (a) and in the solid (b), $Re_h = 544$, $Q = 125$ W.

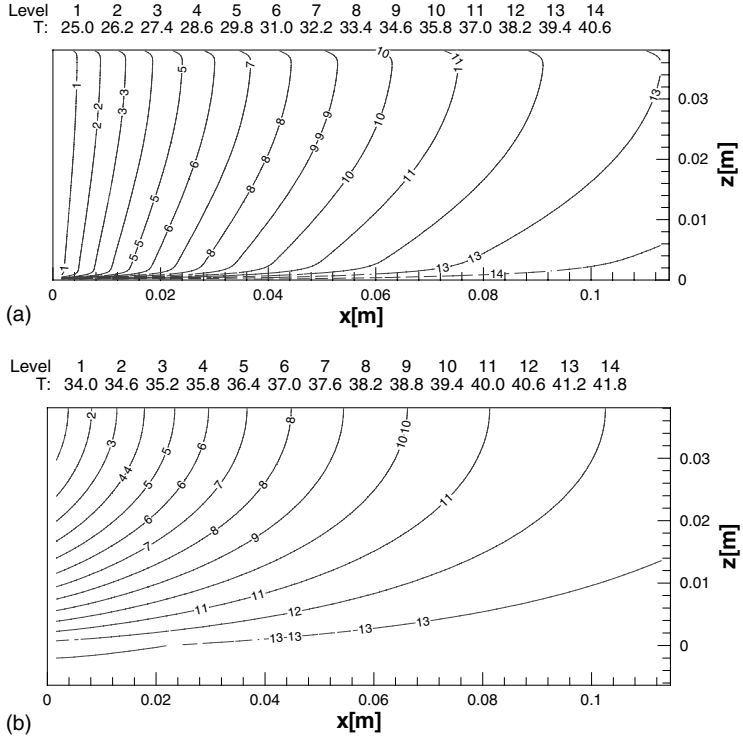

Fig. 11. Temperature field in the fluid (a) and in the solid (b), $Re_h = 768$, $Q = 125$ W.

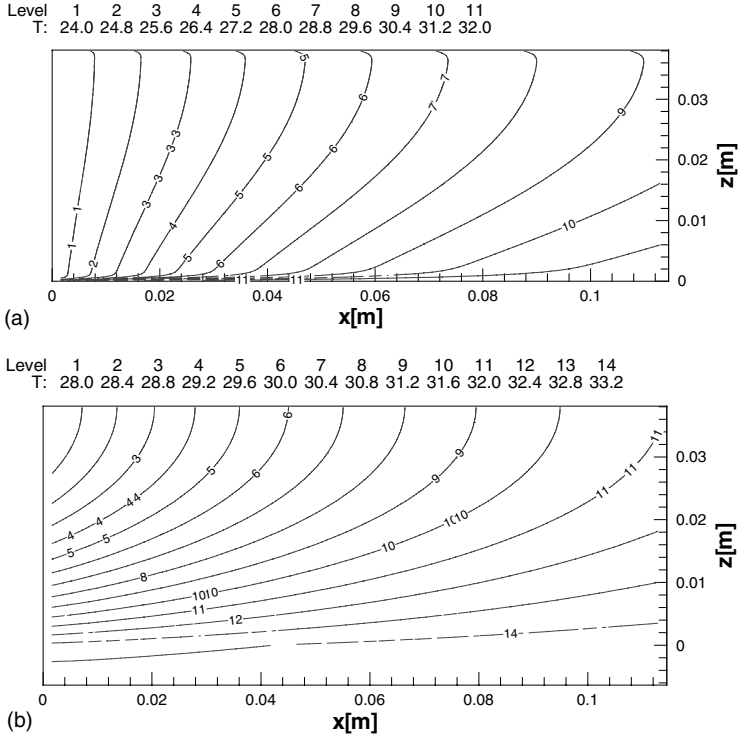

Fig. 12. Temperature field in the fluid (a) and in the solid (b), $Re_h = 1598$, $Q = 125$ W.

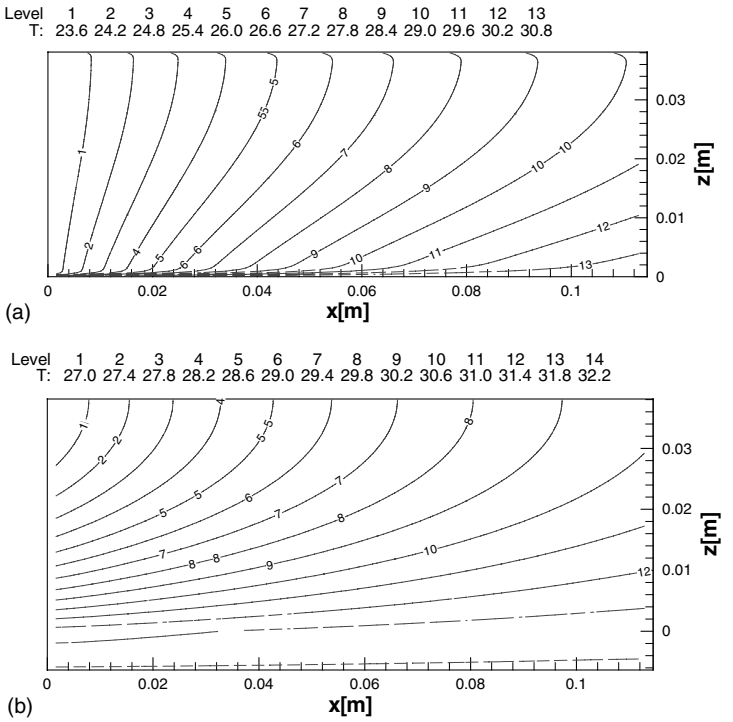

Fig. 13. Temperature field in the fluid (a) and in the solid (b), $Re_h = 1868$, $Q = 125$ W.

Because the heat flux is a vector perpendicular to the isotherms, a qualitative picture of heat flow can be extracted from the calculated temperature fields. It can be seen in Fig. 9 that most of the heat is transferred from the solid to fluid in the first half of the test section. The highest heat fluxes appear in the lower left corner, where the temperature gradients are the largest. The second half of the heat sink still does not participate in the heat transfer process.

Fig. 10 reveals that at low Reynolds number Re_h, the temperature field is not fully developed. This means that air, which enters the test section, is quickly heated due to its low velocity and leaves the heat sink at the temperature of the solid-phase, unable to receive additional heat from the source. With increasing Reynolds number Re_h the state of thermal saturation diminishes (Fig. 10). This heat transfer process also reduces the thermal effectiveness $\overline{Q}/\overline{W}$, as Reynolds number Re_h increases.

The coolant flow unequally lowers the temperature of the heat conducting structure. This directly changes the form of isotherms. The effect is not so evident at low Reynolds numbers (Figs. 8–11). On the contrary, when the Reynolds number Re_h increases, the isotherms become tilted showing the increasing vertical thermal stratification of the coolant flow.

Comparing the temperature fields shown in Figs. 11–13, it can be seen that despite increasing vertical thermal stratification, the flow as well as the solid structure are getting increasingly isothermal. Namely, with the increasing Reynolds number Re_h the airflow leaves the heat sink at lower exit temperature. Such coolant flow is thermally unsaturated, still capable of heat removal. Nevertheless, as the average temperature decreases, the role of heat conducting base-plate increases. This causes further reduction in the air and structure temperatures at the simulation domain exit.

7. Conclusions

The paper represents a contribution to conjugate heat transfer modeling. In this work the VAT was tested and further applied to a simulation of airflow through an aluminum (Al) chip heat sink. The constructed computational algorithm enables prediction of cooling capabilities of the selected geometry. It also offers possibility for geometry improvements to achieve higher thermal effectiveness.

In the frame of performed work, a general form of a porous media flow model was developed using the VAT basic rules. To understand construction of the computational model, the volume averaging procedure was described in details. As the flow variables are averaged over the REV, local momentum and thermal interactions between phases have to be replaced with additional models.

The same averaging procedure was used to develop a specific model for flow through the heat conducting structure of the heat sink. To close the system of the transport equations, the reliable data for intraphase transfer coefficients were found in Launder and Massey [2], Žukauskas and Ulinskas [8], and Kays and London [1]. Using VAT, the computational algorithm is fast running, but still able to present a detailed picture of the temperature field in airflow as well as in the solid structure of the heat sink.

The geometry of the simulation domain and the boundary conditions followed the geometry of the experimental test section used in the Morrin-Martinelli-Gier Memorial Heat Transfer Laboratory at the University of California, Los Angeles. As a calculation technique, the FVM was selected. The calculations were performed at heating power of 50, 125 and 220 W, and at eight different pressure drops. The calculated whole-section drag coefficient $\overline{C}_d$, Nusselt number $\overline{Nu}$ and thermal effectiveness $\overline{Q}/\overline{W}$ were compared with experimental data of Rizzi et al. [34] to verify the computational model and validate the numerical code. The comparison shows a good agreement between the FVM results and the experimental data. The numerical results exhibit up to 10% difference through the whole computational range of Reynolds numbers.

The detailed temperature fields in the coolant flow as well as in the heat conducting structure were also calculated. The calculations revealed that with increasing Reynolds number Re_h the flow thermal saturation decreases. The airflow leaves the heat sink at lower exit temperature, still capable of heat removal. This effect reduces the thermal effectiveness $\overline{Q}/\overline{W}$ of the heat sink. It is also visible that with increasing Reynolds number Re_h the fluid temperature field changes from horizontal to more vertical stratification. As the plotted three-dimensional temperature fields reveal the local heat transfer conditions, they enable corrections and optimization of the heat sink geometry.

The present results demonstrate that the selected VAT approach is appropriate for heat exchanger calculations where thermal conductivity of the solid structure has to be taken into account. The performed calculations also verify that the developed numerical code yields sufficiently accurate results to be applicable also in future optimization calculations for heat exchanger morphologies.

Acknowledgements

A. Horvat gratefully acknowledges the financial support received from the Kerze-Cheyovich scholarship and the Ministry of Education, Science and Sport of Republic of Slovenia. The efforts of I. Catton were the

result of support by DARPA as part of the HERETIC program (DAAD19-99-1-0157).

References

[1] W.S. Kays, A.L. London, Compact Heat Exchangers, third ed., Krieger Publishing Company, Malabar, Florida, 1998, pp. 152–155.

[2] B.E. Launder, T.H. Massey, The numerical prediction of viscous flow and heat transfer in tube banks, J. Heat Transfer 100 (1978) 565–571.

[3] A.A. Johnson, T.E. Tezduyar, J. Lion, Numerical simulations of flows past periodic arrays of cylinders, Comput. Mech. 11 (1983) 371–383.

[4] M. Fujii, T. Fujii, T. Nagata, A numerical analysis of laminar flow and heat transfer of air in an in-line tube bank, Numer. Heat Transfer 7 (1984) 89–102.

[5] G.R. Noghrehkar, M. Kawaji, A.M.C. Chan, Investigation of two-phase flow regimes in tube bundles under cross-flow conditions, Int. J. Multiphase Flow 25 (1999) 857–874.

[6] A. Žukauskas, Heat transfer from tubes in crossflow, Adv. Heat Transfer 8 (1972) 93–160.

[7] A. Žukauskas, Convective Heat Transfer in Cross flow, Handbook of Single-Phase Convective Heat Transfer, Wiley and Sons, New York, 1987.

[8] A. Žukauskas, R. Ulinskas, Efficiency parameters for heat transfer in tube banks, J. Heat Transfer Eng. 5 (1) (1985) 19–25.

[9] K. Al-Jamal, H. Khashashneh, Experimental investigation in heat transfer of triangular and pin fins arrays, Int. J. Heat Mass Transfer 34 (1998) 159–162.

[10] A. Bejan, The optimal spacing for cylinders in crossflow forced convection, J. Heat Transfer 117 (1995) 767–770.

[11] A. Bejan, E. Sciubba, The optimal spacing of parallel plates cooled by forced convection, Int. J. Heat Mass Transfer 35 (12) (1992) 3259–3264.

[12] G. Fabbri, Optimum performances of longitudinal convective fins with symmetrical and asymmetrical profiles, Int. J. Heat Fluid Flow 20 (1999) 634–641.

[13] G. Ledezma, A. Bejan, Heat sinks with sloped plate fins in natural and forced convection, Int. J. Heat Mass Transfer 39 (9) (1996) 1773–1783.

[14] H. Yüncü, G. Anbar, An experimental investigation on performance of rectangular fins on a horizontal base in free convection heat transfer, Heat Mass Transfer 33 (1998) 507–514.

[15] A. Horvat, M. Rizzi, I. Catton, Advanced Computational Methods in Heat Transfer VII: Numerical Investigation of Chip Cooling Using Volume Averaging Technique (VAT), WIT Press, Southampton, UK, 2002, pp. 373–382.

[16] J.E. Hesselgreaves, Compact Heat Exchangers Selection, Design and Operation, Pergamon Press, 2001.

[17] V.S. Travkin, I. Catton, A Two-temperature model for turbulent flow and heat transfer in a porous layer, J. Fluids Eng. 177 (1995) 181–188.

[18] T.B. Anderson, R. Jackson, A fluid mechanical description of fluidized beds, Int. Eng. Chem. Fundam. 6 (1967) 527–538.

[19] J.C. Slattery, Flow of viscoelastic fluids through porous media, AIChE J. 13 (1967) 1066–1071.

[20] C.M. Marle, Ecoulements monophasiquesen milineu poreux, Rev. Inst. Francais du Petrole 22 (1967) 1471–1509.

[21] S. Whitaker, Diffusion and dispersion in porous media, AIChE J. 13 (1967) 420–427.

[22] P.P. Zolotarev, L.V. Redushkevich, The equations for dynamic sorption in an undeformed porous medium, Doklady Phys. Chem. 182 (1968) 643–646.

[23] F.A.L. Dullien, Porous Media Fluid Transport and Pore Structure, Academic Press, New York, 1979.

[24] L.L. Kheifets, A.V. Neimark, Multiphase Processes in Porous Media, Nadra, Moscow, 1982.

[25] P.M. Adler, Porous Media: Geometry and Transport, Butterworth-Heinemann, Stoneham, 1992.

[26] A.V. Primak, A.N. Shcherban, V.S. Travkin, Turbulent Transfer in Urban Agglomerations on the Basis of Experimental Statistical Models of Roughness Layer Morphological Properties, in: Trans. World Meterological Org. Conf. on Air Pollution Modelling and its Application, WMO, Geneve, Switzerland, vol. 2, 1986, pp. 259–266.

[27] A.N. Sheherban, A.V. Primak, V.S. Travkin, Mathamatical Models of Flow and Mass Transfer in Urban Roughness Layer, Problemy Kontrolya i Zaschita Atmosfery or Zagryazneniya 12 (1986) 3–10.

[28] V.S. Travkin, I. Catton, L. Gratton, Single Phase Turbulent Transport in Prescribed Non-Isotropic and Stochastic Porous Media, in: Heat Transfer in Porous Media ASME HTD-240, 1993, pp. 43–48.

[29] V.S. Travkin, L. Gratton, I. Catton, A Morphological Approach for Two-Phase Porous Medium-Transport and Optimum Design Applications in Energy Engineering, in: Proc. 12th Symp. Energy Engin. Sciences, Argonne National Laboratories, Conf.-9404137, 1994, pp. 48–55.

[30] V.S. Travkin, K. Hu, I. Catton, Turbulent Kinetic Energy and Dissipation Rate Equation Models for Momentum Transport in Porous Media, in: Proc. 3rd ASME/JSME Fluids Engineering Conf. FEDSM99-7275, ASME, San Francisco, 1999.

[31] V.S. Travkin, I. Catton, Models of Turbulent Thermal Diffusivity and Transfer Coefficients for a Regular Packed Bed of Spheres, in: Fundamentals of Heat Transfer in Porous Media, ASME HTD-193, 1992, pp. 15–23.

[32] V.S. Travkin, I. Catton, Turbulent Transport of Momentum Heat and Mass in a Two Levels Highly Porous Media, in: Proc. 10th Int. Heat Transfer Conference, vol. 5, Chameleon Press, London, 1994, pp. 399–404.

[33] V.S. Travkin, I. Catton, Transport Phenomena in Heterogeneous Media Based on Volume Averaging Theory, Adv. Heat Transfer 34 (1999) 1–143.

[34] M. Rizzi, M. Canino, K. Hu, S. Jones, V. Travkin, I. Catton, Experimental Investigation of Pin Fin Heat Sink Effectiveness, in: Proc. of the 35th National Heat Transfer Conference, Anaheim, California, 2001.

[35] H.K. Versteeg, W. Malalasekera, An Introduction to Computational Fluid Dynamics, The Finite Volume Method, Longman Scientific and Technical, England, 1995, pp. 103–133.

[36] J.H. Ferziger, M. Perić, Computational Method for Fluid Mechanics, Chapter 5: Solution of Linear Equation Systems, Springer Verlag, Berlin, 1996, pp. 85–127.